Volume 1 | Number 1 | Jan 2013 | Pages 1–100

Journal of
Materials Chemistry A

Materials for energy and sustainability
www.rsc.org/materialsA

ROYAL SOCIETY
OF CHEMISTRY

ROYAL SOCIETY
OF CHEMISTRY

www.rsc.org/materialsA

Journal Name

ARTICLE

Enhanced Photocatalytic Mechanism for the Hybrid g-C$_3$N$_4$/MoS$_2$ Nanocomposite

Jiajun Wang,[a] Zhaoyong Guan,[a] Jing Huang,[a,b] Qunxiang Li[a,*] and Jinlong Yang[a,c]

Here, we explore the enhanced photocatalytic mechanism for the hybrid g-C$_3$N$_4$/MoS$_2$ nanocomposites for the first time by performing extensive density functional theory calculations. The calculated band alignment between g-C$_3$N$_4$ monolayer and MoS$_2$ sheet clearly reveals that the conduction band minimum and valence band maximum of g-C$_3$N$_4$ monolayer is higher about 0.83 eV and 0.15eV than that of MoS$_2$ sheet, respectively. This predicted type-II band alignment ensures the photogenerated electrons easily migrating from g-C$_3$N$_4$ monolayer to MoS$_2$ sheet, and leads to the high hydrogen-evolution reaction activity. The charge transfer between MoS$_2$ and g-C$_3$N$_4$ results in a polarized field within the interface region, which will benefit the separation of photogenerated carriers. The calculated optical absorption curves verify that this proposed layered nanocomposite is a good light-harvesting semiconductor. Moreover, a g-C$_3$N$_4$ bilayer covered on MoS$_2$ sheet also displays desirable properties. These findings indicate that MoS$_2$ sheet is a promising candidate as a non-noble metal co-catalyst for g-C$_3$N$_4$ photocatalyst, and also provide useful information for understanding the observed enhanced photocatalytic mechanism in experiments.

Introduction

The production of chemical fuels by solar energy conversion is an attractive and sustainable solution to the depletion of fossil fuels and the serious environmental problem. H$_2$ will play an important role in this field because it is an ultimate clean energy and can be used in fuel cells.[1–3] Due to the pioneering work of Fujishima and Honda,[4] who demonstrated that overall water splitting can be achieved using a photoelectrochemical cell consisting of a single-crystalline TiO$_2$ anode and a Pt cathode under ultraviolet (UV) irradiation and an external bias, photocatalytic water splitting has been intensively investigated in the past four decades, as a promising strategy for clean, low-cost, and environmentally friendly production of H$_2$ by utilizing solar energy.[5–12] Up to now, most of photocatalysts are discovered in metal oxides, sulfides and nitrides with d^0 or d^{10} transition metal cations.[13] Unfortunately, most of these catalysts are active only under UV irradiation, while others absorbing visible light are not stable during the reaction process, such as photocorrosion in CdS.[6] Photocatalysts for practical use with relatively high productivity are not found yet. Searching for new efficient photocatalysts both from theoretical and experimental aspects is urgently needed.

Metal-free photocatalysts may have the advantage of non-toxicity and good processability, and are gradually becoming an important catalyst. The recent discovered graphitic carbon nitrides (g-C$_3$N$_4$), with a band gap of about 2.7 eV to absorb blue light, have attracted increasing attention for photocatalytic water splitting.[14–19] The g-C$_3$N$_4$ was not only found to be a chemically and thermally stable semiconductor, but also to be capable of achieving both half reactions of water splitting under visible light, meaning that the band-gap covers both the water reduction and water oxidation potentials.[14] However, like many other photocatalysts, the photocatalytic H$_2$ production activity of pristine g-C$_3$N$_4$ remains poor, which strongly relies on the type and amount of surface co-catalysts.[20,21] The co-catalyst can provide reduction or oxidation active sites, catalyze the surface reactions by lowering the activation energies, trapping the charge carriers, and suppressing the recombination of photogenerated electrons and holes.[22] Thus, choosing proper co-catalysts loaded on the light harvesting semiconductor (i.e. g-C$_3$N$_4$) can lead to the nice photocatalytic performance, including activity, selectivity, and stability. In general, the photocatalytic performance always depends on the nature of the light harvesting semiconductor and the functions of the co-catalysts. However, the co-catalysts used are mainly noble metals (i.e. Pt) or their oxides, which are scarce and expensive.[23] Therefore, more attention should be paid for alternative co-catalysts based on non-noble metals.

During the past few years, owing to high hydrogen-evolution reaction (HER) activity for electrocatalyst, molybdenum disulfide (MoS$_2$) with a layered structure has been extensively

investigated as a promising electrocatalyst for H_2 evolution and has been considered as promising alternatives for Pt due to their high abundance and low cost.[24-31] To date, MoS_2 sheet as a co-catalyst for photocatalytic H_2 production has received a lot of experimental attention. For instance, Zong *et al.*[32] have showed the photocatalytic H_2 production activity of CdS could be enhanced by loading MoS_2 sheet. Xiang *et al.*[33] have reported that the Ti-based composite photocatalysts containing a layered MoS_2/graphene co-catalyst afford an effective photocatalyst for H_2 production. Such enhanced photocatalytic performance have been ascribed to the synergistic effects caused by the interfacial interaction between MoS_2 sheet and photocatalyst. Most recently, Hou *et al.*[34] have designed earth-abundant organic-inorganic layered heterojunctions by gas-controlled growth of thin layered MoS_2 on a mesoporous g-C_3N_4 surface. These hybrid junctions exhibited enhanced photocatalytic hydrogen evolution activity under visible-light irradiation, and their performance was comparable to that of Pt/g-C_3N_4 under their reaction conditions. According to these experimental results, it seems that MoS_2 sheet can serve as a suitable co-catalyst to compose with light harvesting semiconductor and show enhanced photocatalytic performance. However, the atomic details at the interface between MoS_2 sheet and light harvesting semiconductor remain poorly understood. And there is still lack of fundamental understanding about the effects of interfacial composition and the mechanisms behind such photocatalysis enhancement of light harvesting semiconductor modified by MoS_2.

Here, we perform extensive density functional (DFT) calculations to characterize the interface between g-C_3N_4 and MoS_2 sheet, and then to clarify the underlying mechanism of enhancing photocatalytic performance. We find that there is somewhat charge transfer from g-C_3N_4 to MoS_2, forming a polarized filed around the interface region. This leads to the enhanced photocatalytic efficiency through reducing e⁻-h⁺ pair recombination. Moreover, our calculations clearly reveal that nearly perfect band alignment exists between g-C_3N_4 (both mono- and bilayer) and MoS_2 sheet. These photogenerated electrons can easily migrate from g-C_3N_4 layer(s) to MoS_2 sheet, which ensures the high HER activity. Moreover, the theoretical findings obtained in this work can be used to understand the experimental results, which can also be extended for future studies of other layered junctions.

Computational details

Our DFT calculations are performed by using the Vienna ab-initio simulation package (VASP).[35,36] The interaction between the core and valence electrons is described using the frozen-core projector augmented wave approach.[37] To optimize their geometric structures, the generalized gradient approximation of Perdew-Burke-Ernzerhof (PBE) form[38] with van der Waals (vdW) correction proposed by Grimme[39,40] is chosen due to its good description of long-range vdW interaction.[41,42] The energy cutoff is set to be 520 eV. A Monkhorst-Pack mesh of[43] $2\times2\times1$ and $6\times6\times1$ k-points is used to sample the two-dimensional Brillouin zone for geometry optimizations and electronic structure calculations, respectively. The vacuum space is set to

be at least 15 Å to separate the interactions between neighboring slabs. All geometry structures are fully relaxed until the convergence criteria of energy and force is less than 10^{-5} eV and 0.01 eV/ Å, respectively.

The band alignment between g-C_3N_4 and layer MoS_2 sheet is one central issue of this study. Considering that in general the PBE functional underestimates the band gaps of semiconductors,[44] all electronic structures are calculated using the Heyd-Scuseria-Ernzerhof (HSE06) hybrid functional.[45] In the default HSE06 functional, the full PBE correlation energy is added, and 1/4 of the PBE exchange is replaced by the Hartree-Fock exact exchange. Namely, the Hartree-Fock exchange mixing parameter (*a*) in the HSE06 functional is set to be 0.25. Unfortunately, the band gap of g-C_3N_4 and MoS_2 sheet is predicted to be 3.19 and 2.14 eV by using the HSE06 functional with *a* = 0.25 (as shown in Figure S1 in Supplementary Information), respectively, which are seriously overestimated.[18,47,48] In order to reproduce the experimental band gaps of isolated g-C_3N_4 and MoS_2 sheets, the value of *a* is decreased from 0.25 to 0.175 in the present work.

To explore the optical properties of g-C_3N_4/MoS_2 nanocomposites, the optical absorption spectra are simulated by converting the complex dielectric function to the absorption coefficient α_{abs} according to the following relation,[46]

$$\alpha_{abs} = \sqrt{2}\omega\left(\sqrt{\varepsilon_1^2(\omega) + \varepsilon_2^2(\omega)} - \varepsilon_1(\varepsilon)\right)^{\frac{1}{2}}$$

where $\varepsilon_1(\omega)$ and $\varepsilon_2(\omega)$ are the real and imaginary parts of frequency dependent complex dielectric function $\varepsilon(\omega)$, respectively. Taking into account the tensor nature of the dielectric function, $\varepsilon_1(\omega)$ and $\varepsilon_2(\omega)$ are averaged over three polarization vectors (along x, y, and z directions).

Results and discussion

Before investigating g-C_3N_4/MoS_2 nanocomposite, we firstly examine the isolated g-C_3N_4 and MoS_2 sheets. In our calculations, the lattice constant of free MoS_2 and g-C_3N_4 is predicted to be 3.19 and 4.79 Å, respectively, which agree well with previous experimental measurements and theoretical results.[18,47,48] For a g-C_3N_4 monolayer, due to the different chemical environments, N atoms are divided into two kinds (N1 and N2), where N1 atoms are fully saturated by the surrounding C atoms, while N2 atoms only connect two C atoms, leaving a non-bonding character, while all C atoms have three nearest-neighbor N atoms, as shown in Fig. 1(a). The C-N1 and C-N2 distances are 1.47 and 1.33 Å, respectively. The calculated band structure and density of states (DOS) of g-C_3N_4 monolayer is plotted in Fig. 1(b) and (c), respectively. Clearly, a g-C_3N_4 sheet is a semiconductor with a direct energy gap of 2.7 eV. The electrons of N1 and C atoms only occupy the states far away from the valence band maximum (VBM), and the VBM is dominated by the N2 atoms. And the calculated partial DOS (PDOS) well reflects the different chemical bonding environment. These observations are close to the previous reports.[18]

The top and side views of optimized MoS_2 sheet with honeycomb structure analogy to graphene are illustrated in Fig.

1(d) and Fig. 1(e), and its DOS and absorption coefficients are presented in Fig. 1 (f) and Fig. 1 (g), respectively. We find that the ground state of MoS_2 sheet is a semiconductor with a direct band gap energy of 2.0 eV, and the Mo-S bond length is 2.42 Å and the vertical S-S distance (d) is 3.13 Å. These results are consistent with the previous works.[49-52] By analyzing the PDOS of MoS_2 sheet, we can see that the electronic states near the conduction band minimum (CBM) and VBM are all mainly contributed by Mo $4d$ orbitals and the S $3p$ orbitals. Moreover, there is a strong hybridization between the Mo $4d$ orbitals and the S $3p$ orbitals, which leads to a large splitting between the bonding and anti-bonding states. As shown in Fig. 1(g), the
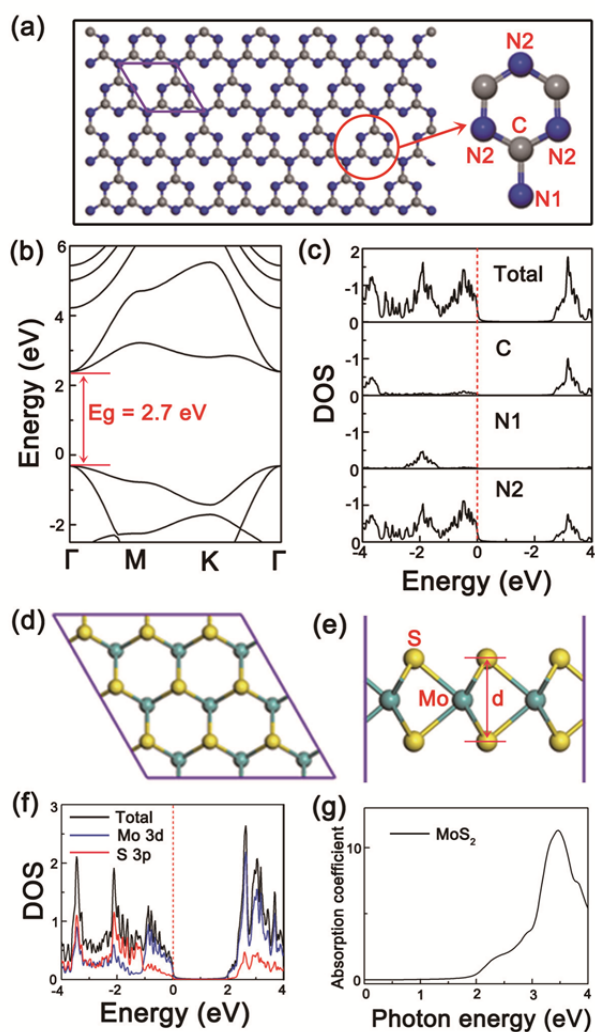
Fig. 1 (a) g-C_3N_4 monolayer. Here, the purple lines show the unit cell in our calculations, the gray and blue balls stand for C and N atoms, respectively. (b) The corresponding calculated band structure, and (c) PDOS of g-C_3N_4 monolayer. (d) The top and (e) side views of MoS_2 sheet. Here, the green and yellow balls stand for Mo and S atoms, respectively. (f) The corresponding calculated PDOS, (g) Absorption coefficients of of MoS_2 sheet.

optical absorption of MoS_2 sheet increases significantly with photon energy over the range of visible light and reaches a maximum absorption at 3.4 eV, which agree well with pervious results.[53] This absorption peak arises from the optical transition

between the valence band (VB) and conduction band (CB) around the K point. It should be pointed out that MoS_2 sheet seems to have a suitable band gap with visible light response, however, it is not an excellent material for water splitting due to the photocorrosion, which always is a demerit point of metal sulfide materials.[6]

To understand the enhanced photocatalytic activity of g-C_3N_4/MoS_2 nanocomposite under visible light irradiation observed in experiments,[34] we propose g-C_3N_4/MoS_2 nanocomposite model, in which a 3×3 supercell of MoS_2 sheet is used to match a 2×2 cell of g-C_3N_4 monolayer, and the lattice mismatch is less than 1.0 %. The top and side views of g-C_3N_4/MoS_2 nanocomposite is shown in Fig. 2(a) and (b), respectively. Due to the presence of MoS_2 sheet, g-C_3N_4 displays obvious geometric distortion, as shown in Fig. 2(b). The corresponding buckling distances (h1) is about 0.92 Å. The vertical separation (h2) between MoS_2 sheet and g-C_3N_4 monolayer is predicted to be 2.97 Å, which is a typical vdW equilibrium spacing. These results are consistent with the previous results.[54,55] To address the interaction between g-C_3N_4 monolayer and MoS_2 sheet, we calculate the interface adhesion energy, which is defined as $E_b = E_{g\text{-}C3N4/MoS2}$ - E_{MoS2} - $E_{g\text{-}C3N4}$, here, $E_{g\text{-}C3N4/MoS2}$, E_{MoS2}, and $E_{g\text{-}C3N4}$ is the total energy of the relaxed g-C_3N_4/MoS_2 nanocomposite, MoS_2, and g-C_3N_4 layers, respectively. The negative E_b denotes that the interface structure between MoS_2 and g-C_3N_4 layers is stable. The E_b is predicted to be -1.41 eV for the examined g-C_3N_4/MoS_2 nanocomposite, which is comparable with these recent theoretical predictions in other g-C_3N_4-based nanocomposites, such as graphene/g-C_3N_4 and g-C_3N_4/$ZnWO_4$ systems,[54,56] indicating that g-C_3N_4 monolayer strongly interacts with MoS_2 sheet, and the corresponding nanocomposite is stable.
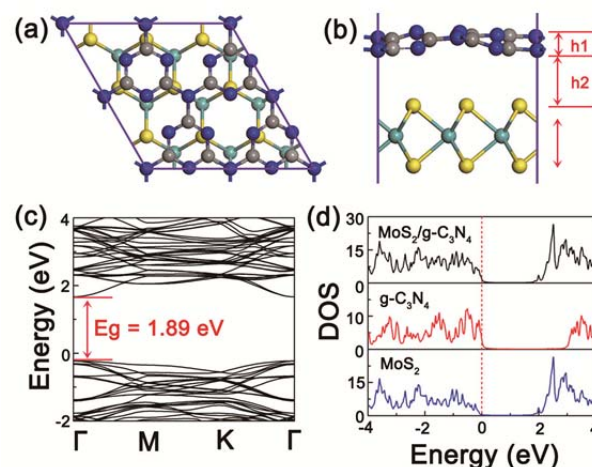
Fig. 2 (a) The top view of the proposed g-C_3N_4/MoS_2 nanocomposite, (b) The side view. (c) The calculated band structure, (d) TDOS and PDOS of g-C_3N_4/MoS_2 nanocomposite. Here, the red and blue lines stand for the PDOS of g-C_3N_4 monolayer and MoS_2 sheet, respectively. The Fermi level is set to zero for clarity.

To describe the g-C_3N_4-MoS_2 interaction more clearly, it is insightful to analyse their electronic structures. The band structure and total DOS of g-C_3N_4/MoS_2 nanocomposite as well as the PDOS of MoS_2 and g-C_3N_4 monolayers are plotted in Fig. 2(c) and (d), respectively. Comparing with the band gaps of g-

C_3N_4 (2.7 eV) and MoS_2 sheet(2.0 eV), the band gap of g-C_3N_4/MoS_2 nanocomposite is reduced to be about 1.89 eV due to the g-C_3N_4-MoS_2 interaction. It implies that the electrons transfer from VB to CB in g-C_3N_4/MoS_2 nanocomposite becomes more easy. Consequently, this results in the red shift of the optical absorption edge.

As shown in Fig. 2(d), the main shape of the calculated DOS projected on two different layers in the proposed hybrid nanocomposite is similar to that of the TDOS of isolated MoS_2 and the g-C_3N_4 monolayers, as shown in Fig. 1(c) and (e), respectively. This is easy to understand, since the separation between MoS_2 and g-C_3N_4 layers (2.97 Å) is relative large, which indicates that the g-C_3N_4-MoS_2 interaction is not very strong due to the absence of covalent bonding upon formation of this hybrid interface. We find that the intrinsic band gap of g-C_3N_4 monolayer in the nanocomposite (2.68 eV) has a tiny change, compared with that of the isolated g-C_3N_4 layer (2.70 eV). It implies that the electron transfer from the N $2p$ at the VB to C $2p$ and N $2p$ at the CB is the dominant process, which excludes the band gap narrowing effect of g-C_3N_4 on improving the hydrogen-production performance.

Moreover, Fig. 2(d) clearly indicates that the band gap of g-C_3N_4 in nanocomposite spans from 0.0 to 2.68 eV, and MoS_2 has a 2.0 eV band gap spanning from -0.15 to 1.85 eV. The top part of the VB is mainly contributed by g-C_3N_4, while the states from MoS_2 sheet locate at the relative low position (0.15 eV). This indicates that the valence band offset (VBO) between g-C_3N_4 and MoS_2 is about 0.15 eV. On the other hand, the bottom part of the CB mainly comes from the states of MoS_2 sheet, while the position of the states from g-C_3N_4 are high about 0.83 eV, which means that the conduction band offset (CBO) between g-C_3N_4 and MoS_2 is about 0.83 eV. These observations imply that once g-C_3N_4 monolayer is covered on MoS_2 sheet, the band alignment between the two layered materials results in the formation of type-II heterojunction.[57,58] This is the first key finding to understand the enhanced photoactivity of the proposed g-C_3N_4/MoS_2 nanocomposite, which will discuss in more details in below context. Note that this finding is not sensitive to the adopted functional in DFT calculations. Both PBE and HSE06 functionals calculations show type-II band alignment, although the absolute values of the band gaps of MoS_2 and g-C_3N_4 monolayers depend on the used functional (Figure S2 and S3 in Supplementary Information).

To explore the charge transfer process in g-C_3N_4/MoS_2 nanocomposite, the charge density difference obtained by subtracting the electronic charge of a hybrid g-C_3N_4/MoS_2 nanocomposite from that of the free MoS_2 and g-C_3N_4 monolayers are calculated and shown in Fig. 3. Here, the red and blue colors represent charge accumulation and depletion, respectively. It is clear that the charge redistribution mainly occurs at the interface region. Although the large separation between the g-C_3N_4 and MoS_2 sheet leads to the weak donor-acceptor coupling, there is somewhat charge transfer from the g-C_3N_4 to the MoS_2 sheet. That is to say, the holes accumulate in the g-C_3N_4 region, while the electrons accumulate in the region close to MoS_2 sheet. Therefore, in the junction region a polarized field is generated which points from the g-C_3N_4 to

MoS_2 sheet. This is the second key finding, which can prevent the recombination of photogenerated electrons and holes. Moreover, with help of this nice separation of e$^-$-h$^+$ pairs, the lifetime of photoinduced carriers is effectively prolonged, which is beneficial for photocatalysis. In this sense, MoS_2 sheet shows a positive effect on the photocatalytic performance of g-C_3N_4/MoS_2 nanocomposite.
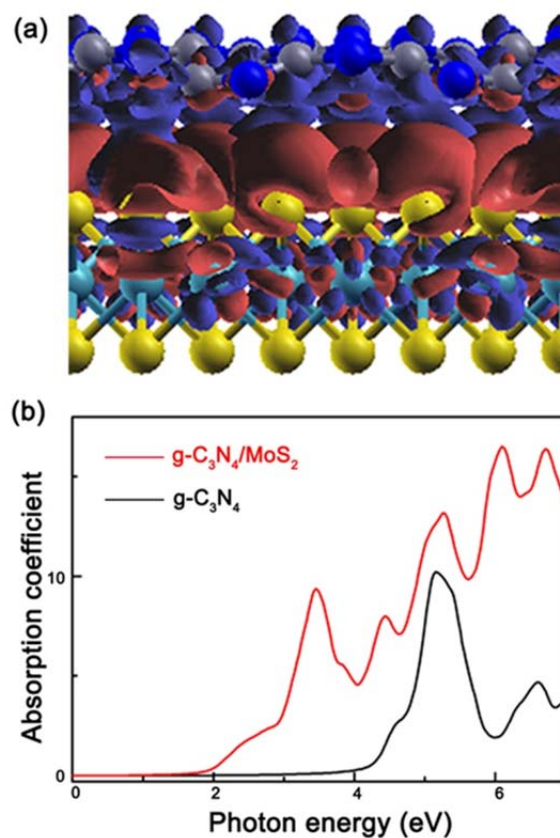
Fig. 3 (a) Charge density differences in g-C_3N_4/MoS_2 nanocomposite. The red and blue regions represents charge accumulation and depletion, respectively, and the isosurface value is 0.001 e/Å^3. (b) The calculated Absorption coefficients of g-C_3N_4 monolayer and g-C_3N_4/MoS_2 nanocomposite, which is labeled with the black and red lines, respectively.

To examine the combination effect of g-C_3N_4 sheet and MoS_2 sheet, the optical absorption curves of g-C_3N_4 monolayer and the hybrid g-C_3N_4/MoS_2 nanocomposite are calculated and plotted in Fig. 3(b) with the black and red lines, respectively. In general, the optical absorption property of a semiconductor photocatalyst, a key factor in determining its photocatalytic activity, is strong related to its electronic structures.[59] As shown in Fig. 3(c), g-C_3N_4 monolayer has a moderate direct energy gap (2.7 eV), which should be a suitable visible-light absorber. However, we find that g-C_3N_4 monolayer has absorption above 4.0 eV, which is significant larger than the direct energy gap at the Γ point. A similar phenomenon has been observed by Wu *et al.*[60] They suggested that the orbital overlap and the optical transitions between CBM and VBM are negligible, leading to light absorption in a high energy region. One can expect that g-C_3N_4/MoS_2 nanocomposite should display improved optical

properties when g-C$_3$N$_4$ layer is covered on MoS$_2$ sheet. This is verified by the calculated optical adsorption curve of g-C$_3$N$_4$/MoS$_2$ nanocomposite, as shown in the Fig. 3(b). Clearly, compared with g-C$_3$N$_4$ monolayer, the proposed hybrid nanocomposite exhibits more effective UV absorption and enhanced low-energy visible light response. Red shift of the absorption edge is as large as 2.0 eV for g-C$_3$N$_4$/MoS$_2$ nanocomposite because electron can be directly excited from the VB of g-C$_3$N$_4$ layer to the CB of MoS$_2$ sheet.

From the above presented DOSs of the proposed MoS$_2$/g-C$_3$N$_4$ nanocomposite nanocomposite, the band alignment is illustrated in Fig. 4. Clearly, g-C$_3$N$_4$/MoS$_2$ nanocomposite is a type-II heterojunction.[57,58] The CB and VB of g-C$_3$N$_4$ monolayers are more positive than the corresponding bands of MoS$_2$ sheet. Thus, when this proposed nanocomposite is illuminated with light, the electrons can be photonexcited from the CB of both MoS$_2$ and g-C$_3$N$_4$ monolayers. Note that these photogenerated electrons in g-C$_3$N$_4$ layer can be easily moved to the CB of MoS$_2$ sheet due to the observed CBO. Since MoS$_2$ sheet has sufficient chemical potential for the electrons to react with protons to produce hydrogen at HER active sites,[24-31] thus these photogenerated electrons can be effectively utilized. On the other hand, the VBM offset between the two layered materials provides the redistribution of electrons and holes, as shown in Fig. 3(a). That is to say, the oxidation and redox reactions could take place in g-C$_3$N$_4$ and MoS$_2$ sheets, respectively. At the same time, the energy-wasteful e$^-$-h$^+$ recombination could be greatly reduced.
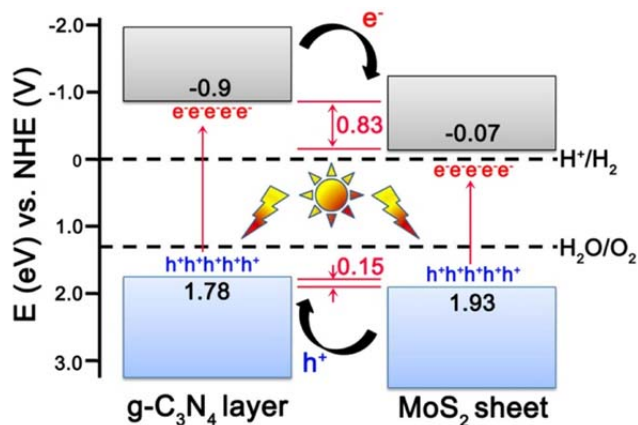
Fig. 4 Schematic illustration of the carriers transfer and separation in the proposed g-C$_3$N$_4$/MoS$_2$ nanocomposite.

It should be pointed out that the polarized field between g-C$_3$N$_4$ and MoS$_2$ sheets in the nanocomposite prevents the photogenerated electrons migrating from g-C$_3$N$_4$ monolayer to MoS$_2$ sheet. Therefore, there is a competitive role in electron-hole separation between the band alignment and electric polarized field. According to the estimated values, we find that the electric field strength coming from the band alignment, as shown in Fig. 4, is about three times larger than that of the dipole-induced polarized field (see Supplementary Information). This indicates that the migration of photogenerated electrons in g-C$_3$N$_4$/MoS$_2$ nanocomposite is dominated by the strong driving force provided by the type-II band alignment.

As one of typical metal sulfide photocatalysts, MoS$_2$ can be photocorroded under band gap excitation since the S^{2-} in MoS$_2$ photocatalysts rather than H$_2$O is oxidized by photogenerated holes.[6] As shown in Fig. 4, the photogenerated holes in MoS$_2$ sheet can easily move to g-C$_3$N$_4$ monolayer in g-C$_3$N$_4$/MoS$_2$ nanocomposite due to the type-II band alignment. This may well resolve the photocorrosion problem of MoS$_2$ sheet in this proposed nanocomposite. These findings reveal that MoS$_2$ is a promising candidate as a non-noble metal co-catalyst for g-C$_3$N$_4$ photocatalyst, which can rationalize the significant enhancement of visible light photoactivity of g-C$_3$N$_4$ by growing with MoS$_2$ sheets.[34]
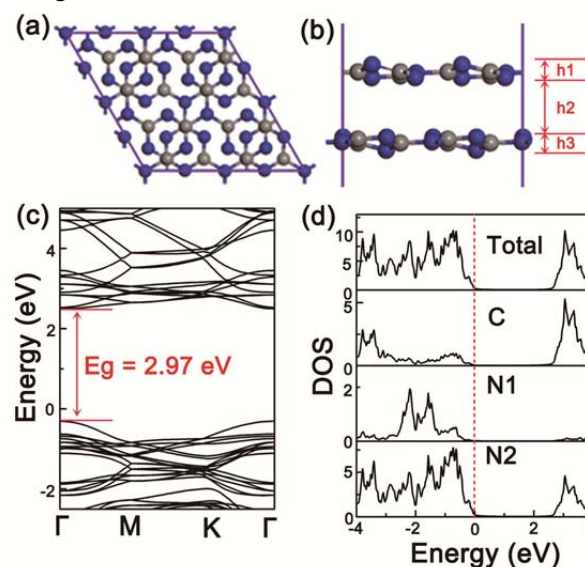
Fig. 5 (a) The top view of BL-g-C$_3$N$_4$, (b) The side view, (c) The corresponding calculated band structure, (d) The TDOS of BL-g-C$_3$N$_4$ and PDOS of C and N1 and N2 atoms.

Above, we focus on the hybrid nanocomposite with a g-C$_3$N$_4$ monolayer covered on MoS$_2$ sheet. Actually, g-C$_3$N$_4$ synthesized in experiments is usually nanometer-scale thickness, which includes a few atomic layers.[14,18] Thus, an interesting question is whether the type-II band alignment happens or not when the number of g-C$_3$N$_4$ atomic layer increases. Firstly, we investigate the geometric and electronic structures of g-C$_3$N$_4$ bilayer (labelled with BL-g-C$_3$N$_4$) as an example. Eight kinds of nonequivalent structures of BL-g-C$_3$N$_4$ according to the different symmetries are examined. Among them, the top and side views of the most stable structure of BL-g-C$_3$N$_4$ is shown in Fig. 5(a) and Fig. 5(b), respectively. The corresponding buckling distances of top layer (h1) and bottom layer (h3) are both about 0.70 Å, which are smaller than that of g-C$_3$N$_4$ monolayer (0.92 Å). The vertical distance between two g-C$_3$N$_4$ layers is about 2.57 Å. And the corresponding binding energy is predicted to be 0.67 eV, indicating a relative strong chemical bonding between two g-C$_3$N$_4$ layers. This is totally different with the weak interactions in other two-dimensional bilayers, such as graphene bilayer[61] and a graphene/BN bilayer.[62] To explore the stacking effect in the most stable g-C$_3$N$_4$ bilayer, we calculate its band structure and PDOS of g-C$_3$N$_4$ bilayer, as shown in Fig. 5(c) and Fig. 5(d), respectively. It is clear that the BL-g-C$_3$N$_4$ displays semiconducting character with a direct

energy gap (2.97 eV), and its band gap is enlarged about 0.27 eV compared with g-C$_3$N$_4$ monolayer (2.7 eV).

Then, we turn to examine BL-g-C$_3$N$_4$ loading on MoS$_2$ sheet. The top and side views of this new proposed nanocomposite are illustrated in Fig. 6(a) and Fig 6(b), respectively. Due to the presence of MoS$_2$ sheet, BL-g-C$_3$N$_4$ displays obvious geometric change. The corresponding buckling distances of top layer (h1) and bottom layer (h3) of BL-g-C$_3$N$_4$ are about 0.83 and 0.81 Å, respectively, while the distance (h2) between the two g-C$_3$N$_4$ layers is 2.29 Å, which is smaller than that of g-C$_3$N$_4$ monolayer (2.57 Å). A typical vdW equilibrium space (h4) between BL-g-C$_3$N$_4$ and MoS$_2$ sheet is about 3.16 Å, which is slight larger than that of g-C$_3$N$_4$ monolayer loading on MoS$_2$ sheet (2.97 Å), as shown in Fig. 2(a). This observation is consistent with the slight small interface adhesion energy (-1.37 eV) of BL-g-C$_3$N$_4$ covered on MoS$_2$ sheet. To analyze the carrier migration path in the interface between BL-g-C$_3$N$_4$ and MoS$_2$ sheet, the TDOS and PDOS projected on individual MoS$_2$ and BL-g-C$_3$N$_4$ in this BL-g-C$_3$N$_4$/MoS$_2$ nanocomposite are presented in Fig. 6(c). Similar to the first proposed g-C$_3$N$_4$/MoS$_2$ nanocomposite, the band alignment of BL-g-C$_3$N$_4$/MoS$_2$ nanocomposite shows that it is also a type-II heterojunction. It is clear that the CB (VB) edge of BL-g-C$_3$N$_4$ is higher than the CB (VB) edge of MoS$_2$ sheet. There is a band gap of about 1.98 eV between the VB edge of BL-g-C$_3$N$_4$ and the CB edge of MoS$_2$ sheet. The obtained band structures provide the possibility of the directional migration of photogenerated electrons from BL-g-C$_3$N$_4$ to MoS$_2$ sheet, and this offers the sufficient chemical potential for the photogenerated electrons to react with protons to produce hydrogen at HER active sites of MoS$_2$ sheet.[24-31]
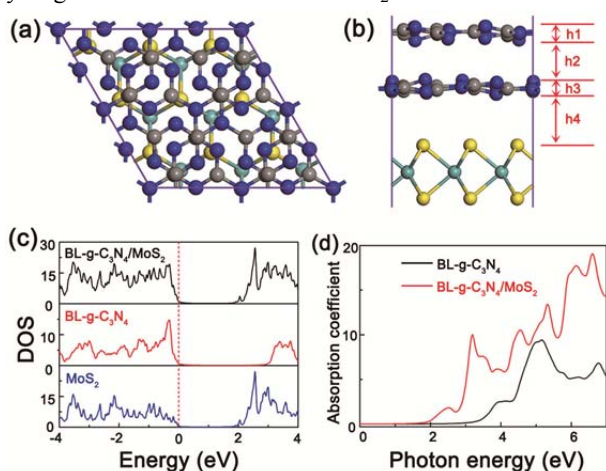
Fig. 6 (a) The top view of BL-g-C$_3$N$_4$/MoS$_2$ nanocomposite, (b) The side view, (c) The corresponding TDOS of BL-g-C$_3$N$_4$/MoS$_2$ nanocomposite, and the PDOS of BL-g-C$_3$N$_4$/MoS$_2$ and MoS$_2$ sheet are plotted with the black, red and blue lines, respectively. The Fermi level is set to zero for clarity. (d) The optical adsorption spectra of BL-g-C$_3$N$_4$ and BL-g-C$_3$N$_4$/MoS$_2$ nanocomposite, which is labeled with the black and red lines, respectively.

Finally, we calculate the absorption spectrum of BL-g-C$_3$N$_4$ and BL-g-C$_3$N$_4$/MoS$_2$ nanocomposite and plot them in Fig. 6(d). Comparing to g-C$_3$N$_4$ monolayer loading on MoS$_2$ sheet, we find that the covered BL-g-C$_3$N$_4$ has much better optical

absorption below 3.0 eV. This agrees well with the previous results,[60] which reported that the interlayer coupling modifies the orbital, leading to stronger overlap of CBM and VBM of BL-g-C$_3$N$_4$. Thus, it improves the visible-light absorption. As seen in Fig. 6(d), this examined BL-g-C$_3$N$_4$/MoS$_2$ nanocomposite indeed displays expanded optical absorption from UV into visible light, which can efficiently harvest a broad range of visible light.

Conclusions

In summary, we perform extensive DFT calculations to explore the enhanced photocatalytic mechanism for the hybrid MoS$_2$/g-C$_3$N$_4$ nanocomposites, including both g-C$_3$N$_4$ mono- and bilayer loading on MoS$_2$ sheet. The calculated band alignment between g-C$_3$N$_4$ monolayer and MoS$_2$ sheet reveals that the CBM (VBM) of g-C$_3$N$_4$ is higher about 0.83 eV (0.15 eV) than that of the CBM (VBM) of MoS$_2$ sheet. This predicted type-II band alignment ensures the photogenerated electrons can easily migrate from g-C$_3$N$_4$ layer to MoS$_2$ sheet, and leads to high HER activity. The charge transfer between MoS$_2$ and g-C$_3$N$_4$ results in a polarized filed within the interface region, which can effectively improve the separation efficiency of these photogenerated carriers. In addition, this hybrid layered junction has high light absorption ability. Similar results are also obtained for a g-C$_3$N$_4$ bilayer covered on MoS$_2$ sheet. These theoretical predictions provide insight to understand the related experimental observations, and verify that MoS$_2$ sheet is a promising candidate as a non-noble metal co-catalyst for g-C$_3$N$_4$ photocatalyst.

Notes and references

^{a} *Hefei National Laboratory for Physical Sciences at the Microscale, University of Science and Technology of China, Hefei, Anhui 230026, China. E-mail: liqun@ustc.edu.cn*
^{b} *School of Materials and Chemical Engineering, Anhui Jianzhou University, Hefei, Anhui 230022, China.*
^{c} *Synergetic Innovation Center of Quantum Information and Quantum Physics, University of Science and Technology of China, Hefei, Anhui 230026, China.*

† Electronic Supplementary Information (ESI) available: The calculated band structures with different exchange mixing parameters, the DOS and PDOS of of g-C$_3$N$_4$/MoS$_2$ nanocomposite and its band alignment at the PBE level, INCAR and POSCAR files. See DOI: 10.1039/b000000x/

1   J. A. Turner, *Science*, 1999, **285**, 687-689.
2   M. S. Dresselhaus and I. L. Thomas, *Nature*, 2001, **414**, 332-337.
3   N. S. Lewis and D. G. Nocera, *Proc. Natl. Acad. Sci. U.S.A.*, 2006, **103**, 15729-15735.

4   A. Fujishima and K. Honda, *Nature*, 1972, **238**, 37-38.
5   K. Maeda and K. Domen, *J. Phys. Chem. C*, 2007, **111**, 7851-7861.
6   A. Kudo and Y. Miseki, *Chem. Soc. Rev.*, 2009, **38**, 253-278.
7   X. Chen, S. Shen, L. Guo and S. S. Mao, *Chem. Rev.*, 2010, **110**, 6503-6570.
8   K. Maeda and K. Domen, *J. Phys. Chem. Lett.*, 2010, **1**, 2655-2661.
9   N. Serpone and A. V. Emeline, *J. Phys. Chem. Lett.*, 2012, **3**, 673-677.
10 H. Tong, S. Ouyang, Y. Bi, N. Umezawa, M. Oshikiri and J. Ye, *Adv. Mater.*, 2012, **24**, 229-251.
11 K. Maeda, *Phys. Chem. Chem. Phys.*, 2013, **15**, 10537-10548.
12 F. E. Osterloh, *Chem. Soc. Rev.*, 2013, **42**, 2294-2320.
13 Y. Inoue, *Energy Environ. Sci.*, 2009, **2**, 364-386.
14 X. Wang, K. Maeda, A. Thomas, K. Takanabe, G. Xin, J. M. Carlsson, K. Domen and M. Antonietti, *Nat. Mater.*, 2009, **8**, 76-80.
15 G. Liu, P. Niu, C. Sun, S. C. Smith, Z. Chen, G. Q. Lu and H.-M. Cheng, *J. Am. Chem. Soc.*, 2010, **132**, 11642-11648.
16 Y. Zhang, T. Mori, J. Ye and M. Antonietti, *J. Am. Chem. Soc.*, 2010, **132**, 6294-6295.
17 Y. Wang, J. Zhang, X. Wang, M. Antonietti and H. Li, Angew. *Chem. Int. Ed.*, 2010, **49**, 3356-3359.
18 G. Dong, K. Zhao and L. Zhang, *Chem. Commun.*, 2012, **48**, 6178-6180.
19 J. Zhang, M. Zhang, R.-Q. Sun and X. Wang, *Angew. Chem. Int. Ed.*, 2012, **51**, 10145-10149.
20 K. Maeda, X. Wang, Y. Nishihara, D. Lu, M. Antonietti and K. Domen, *J. Phys. Chem. C*, 2009, **113**, 4940-4947.
21 Y. Di, X. Wang, A. Thomas and M. Antonietti, *ChemCatChem*, 2010, **2**, 834-838.
22 J. Yang, D. Wang, H. Han and C. Li, *Acc. Chem. Res.*, 2013, **46**, 1900-1909.
23 P. C. K. Vesborg and T. F. Jaramillo, *RSC Adv.*, 2012, **2**, 7933-7947.
24 T. F. Jaramillo, K. P. Jorgensen, J. Bonde, J. H. Nielsen, S. Horch and I. Chorkendorff, *Science*, 2007, **317**, 100-102.
25 D. Merki and X. Hu, *Energy Environ. Sci.*, 2011, **4**, 3878-3888.
26 H. I. Karunadasa, E. Montalvo, Y. Sun, M. Majda, J. R. Long and C. J. Chang, *Science*, 2012, **335**, 698-702.
27 A. B. Laursen, S. Kegnaes, S. Dahl and I. Chorkendorff, *Energy Environ. Sci.*, 2012, **5**, 5577-5591.
28 H. Vrubel, D. Merki and X. Hu, *Energy Environ. Sci.*, 2012, **5**, 6136-6144.
29 T. Wang, L. Liu, Z. Zhu, P. Papakonstantinou, J. Hu, H. Liu and M. Li, *Energy Environ. Sci.*, 2013, **6**, 625-633.
30 Y. Li, H. Wang, L. Xie, Y. Liang, G. Hong and H. Dai, *J. Am. Chem. Soc.*, 2011, **133**, 7296-7299.
31 Z. Chen, D. Cummins, B. N. Reinecke, E. Clark, M. K. Sunkara and T. F. Jaramillo, *Nano Lett.*, 2011, **11**, 4168-4175.
32 X. Zong, H. Yan, G. Wu, G. Ma, F. Wen, L. Wang and C. Li, *J. Am. Chem. Soc.*, 2008, **130**, 7176-7177.
33 Q. Xiang, J. Yu and M. Jaroniec, *J. Am. Chem. Soc.*, 2012, **134**, 6575-6578.
34 Y. Hou, A. B. Laursen, J. Zhang, G. Zhang, Y. Zhu, X. Wang, S. Dahl and I. Chorkendorff, *Angew. Chem. Int. Ed.*, 2013, **52**, 3621-3625.
35 G. Kresse and J. Furthmuller, *Phys. Rev. B.*, 1996, **54**, 11169.
36 G. Kresse and J. Furthmuller, *Comput. Mater. Sci.*, 1996, **6**, 15-50.
37 P. E. Blochl, *Phys. Rev. B.*, 1994, **50**, 17953.
38 J. P. Perdew, K. Burke and M. Ernzerhof, *Phys. Rev. Lett.*, 1996, **77**, 3865.
39 S. Grimme, *J. Comput. Chem.*, 2004, **25**, 1463-1473.
40 S. Grimme, *J. Comput. Chem.*, 2006, **27**, 1787-1799.
41 W. Geng, X. Zhao, H. Liu and X. Yao, *J. Phys. Chem. C*, 2013, **117**, 10536-10544.
42 W. Hu, Z. Li and J. Yang, *J. Chem. Phys.*, 2013, **138**, 124706.
43 H. J. Monkhorst and J. D. Pack, *Phys. Rev. B.*, 1976, **13**, 5188.
44 Perdew, J. P. *Int. J. Quantum Chem.*, 1986, **30,** 451-451.
45 J. Heyd, G. E. Scuseria and M. Ernzerhof, *J. Chem. Phys.*, 2003, **118**, 124706-5.
46 M. Chhowalla, H. S. Shin, G. Eda, L.-J. Li, K. P. Loh and H. Zhang, *Nat. Chem.*, 2013, **5**, 263-275.
47 M. Xu, T. Liang, M. Shi and H. Chen, *Chem. Rev.*, 2013, **113**, 3766-3798.
48 M. Gajdos, K. Hummer, G. Kresse, J. Furthmuller, F. Bechstedt, *Phys. Rev. B.*, 2006, **73**, 045112.
49 C. Ataca, H. Sahin, S. Ciraci, *J. Phys. Chem. C*, 2012, **116**, 8983-8999.
50 C. Ataca, M. Topsakal, E. Akturk, S. Ciraci, *J. Phys. Chem. C*, 2011, **115**, 16354-16361.
51 C. Ataca, S. Ciraci, *Phys. Rev. B.*, 2012, **85**, 195410.
52 Y. Ma, Y. Dai, M. Guo, C. Niu, B. Huang, *Nanoscale*, 2011, **3**, 3883-3887.
53 N. Singh, G. Jabbour, U. Schwingenschlogl, *Eur. Phys. J. B*, 2012, **85**, 1-7.
54 L. Sun, X. Zhao, C.-J. Jia, Y. Zhou, X. Cheng, P. Li, L. Liu and W. Fan, *J. Mater. Chem.*, 2012, **22**, 23428-23438.
55 A. Du, S. Sanvito and S. C. Smith, *Phys. Rev. Lett.*, 2012, **108**, 197207.
56 A. Du, S. Sanvito, Z. Li, D. Wang, Y. Jiao, T. Liao, Q. Sun, Y. H. Ng, Z. Zhu, R. Amal and S. C. Smith, *J. Am. Chem. Soc.*, 2012, **134**, 4393-4397.
57 Z. Alferov, *Semiconductors*, 1988, **32**, 1.
58 J. Tersoff, *Phys. Rev. B.*, 1984, **30**, 4874.
59 Y. Zhu, Y. Dai, K. Lai, Z. Li, B. Huang, *J. Phys. Chem. C*, 2013, **117**, 5593-5598.
60 F. Wu, Y. Liu, G. Yu, D. Shen, Y. Wang and E. Kan, *J. Phys. Chem. Lett*, 2012, **3**, 3330-3334.
61 T. Ohta, A. Bostwick, T. Seyller, K. Horn and E. Rotenberg, *Science,* 2006, **313**, 951-954.
62 E. Kan, H. Ren, F. Wu, Z. Li, R. Lu, C. Xiao, K. Deng and J. Yang, *J. Phys. Chem. C*, 2012, **116**, 3142-3146.
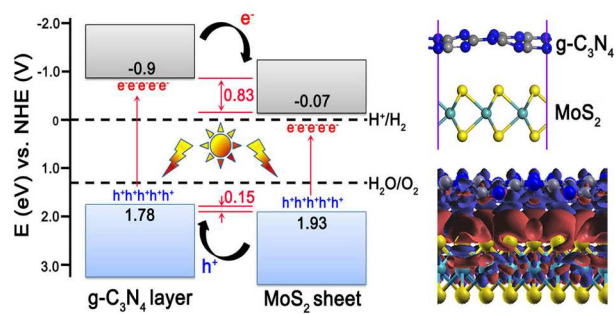
The predicted type-II band alignment and the interfacial polarized field in g-C₃N₄/MoS₂ nanocomposite are responsible for its enhanced photocatalysis.